Investigating the Borromean Nucleus ^{29}F at the Neutron Drip-Line

by Jessica Churchill

April 2016

A Thesis Submitted to Saint Mary's University,
Halifax, Nova Scotia in Partial Fulfillment
of the Requirements for the Degree of Honours Physics.

Supervisor: Dr. Rituparna Kanungo
Department of Astronomy and Physics
Saint Mary's University
Halifax, Nova Scotia

Submitted: April 14th, 2016

Investigating the Borromean Nucleus ^{29}F at the Neutron Drip-Line

by Jessica Churchill

April 14th, 2016

Abstract

A nuclear halo is a nucleus which has a large extended surface region of either one or two protons or neutrons surrounding a compact core nucleus. A Borromean nucleus is a special case consisting of a core surrounded by a two-nucleon halo. This creates a bound system where removing any one of these three major components causes it to break. ^{29}F is a Borromean nucleus, located at Z=9, N=20 on the map of nuclei. In neutron-rich nuclei such as this one, nuclear shell structure may change, and there is evidence to suggest that the magic number N=20 breaks down. Such breakdown has been observed in Mg and Na isotopes. This region is referred to as the N=20 island of inversion. ^{29}F is the most neutron-rich nucleus with N=20. It is therefore important to investigate if the N=20 shell gap breaks down at ^{29}F and whether this Borromean nucleus forms a 2s halo.

To investigate ^{29}F, which has a half-life of only $\approx$ 2.4ms, it has to be produced in a laboratory. To do this, a beam of a stable nucleus must collide with a target, creating many different fragments including ^{29}F. From this, ^{29}F needs to be identified and separated from the other nuclei. Simulation results of how this will be done using the BigRIPS fragment separator and particle detectors at the RIKEN RI Beam Factory in Japan will be discussed in this thesis.

Date:

Contents

1   Introduction

1.1   Magic Numbers and Nuclear Shell Structure

Just over 50 years ago, the Nobel Prize in Physics was awarded to Maria Goeppert Mayer and J. Hans D. Jensen for their discoveries of nuclear magic numbers and shell structure [1]. By examining observables such as nuclear binding energy, beta decay Q-values, energies of first excited states, and neutron capture cross sections of nuclei, they noticed each time that there were discontinuities in the overall trends that continuously reoccurred at the same nucleon numbers [2]. These numbers, referred to as magic numbers, are the proton and neutron numbers 2, 8, 10, 20, 28, 50, 82, and 126 [3]. These numbers correspond to the number of nucleons which form a complete shell within a nucleus and indicate a particularly stable nuclear system [4].

On the map of nuclei, there exists what are referred to as proton and neutron drip-lines, as shown below in Figure 1. These nucleon drip-lines represent the extreme ratios of protons to
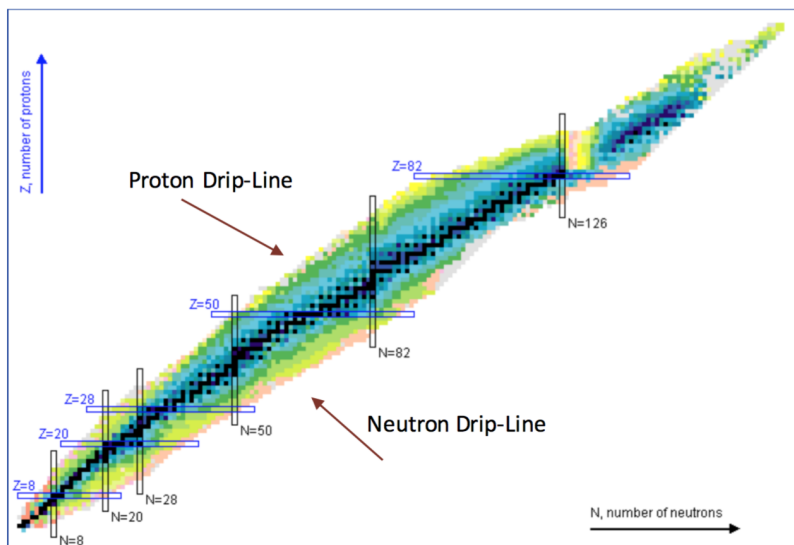

Figure 1: Map of Nuclei, where isotopes are plotted based on their number of protons (Z) and number of neutrons (N) [5].

neutrons, beyond which no stable nuclei can exist [6]. Additional nucleons added beyond this point will drip out of these unstable nuclei. It has been discovered that neutron-rich nuclei, located on or near the neutron drip-line, exhibit unusual properties which bring changes to our knowledge of nuclear shell structure [7].

1.2 Borromean Nuclei

Particularly unique quantum systems are Borromean halo nuclei. These nuclei have a large extended surface region, referred to as a halo [8], consisting of a compact core nucleus surrounded by two nucleons. This creates a bound system where removing any one of these three major components causes it to break. The halo causes the size of the nucleus to be equivalent to that of a much heavier atom, as is shown in Figure 2, so it is therefore much larger than neighbouring isotopes [9]. One such Borromean nucleus is ^{29}F, which contains 9 protons and 20 neutrons (N=20, Z=9), making it a very neutron-rich nucleus. It is located on the neutron drip-line on the map of nuclei at the magic number N=20. This region is referred to as the N=20 island of inversion, which is the region in which N=20 is broken. However, for ^{29}F, it is not yet known if N=20 is broken or not, therefore it needs to be further studied.
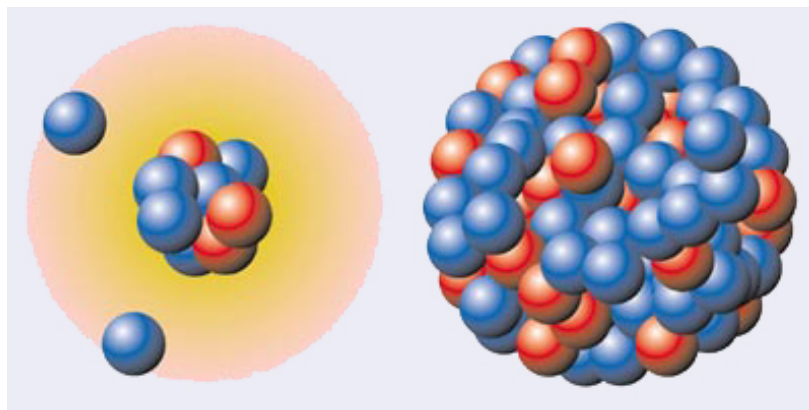

Figure 2: Borromean nucleus with a two-nucleon halo (left) compared to a more typical nucleus (right) [10].

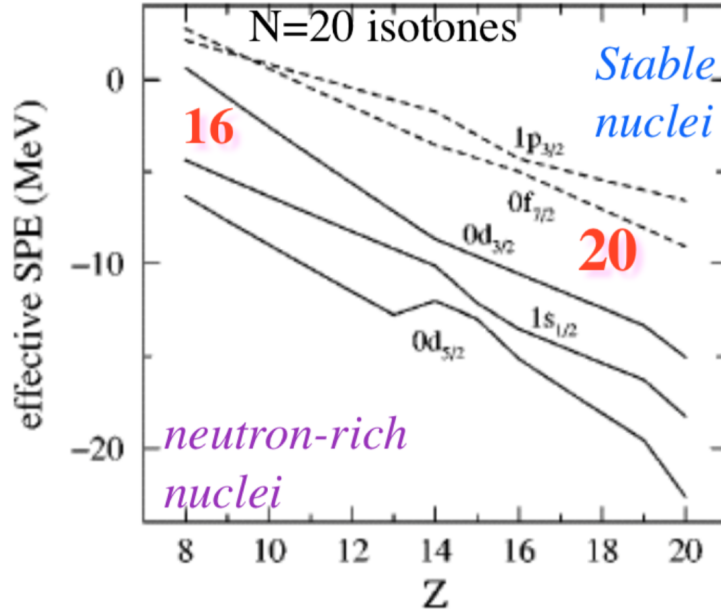## 1.3 Potential Breakdown of the Magic Number N=20

Figure 3: Diagram showing the N=20 shell gap based on a theoretical prediction by a modern shell model calculation in which the lines correspond to the energy of neutron orbitals [11].

There is evidence to suggest that the magic number N=20 could break down for ^{29}F, such as the dominance of an unexpected orbital. This could lead to a breakdown of the shell closure. These orbitals, which are energetically lowered compared to conventional shell model expectations, are referred to as intruder orbitals, as is shown in Figure 3. Such evidence includes the fact that the N=20 magic number is found to disappear in Mg and Na isotopes [12]. The non-existence of ^{28}O (N=20, Z=8) is also suggestive of N=20 breaking down in O [13]. This implies that ^{29}F, which is the last bound N=20 isotope, can be anticipated to have N=20 shell breakdown.

However, recent shell model calculations [12] predict that the intruder orbital component in ^{29}F is small in the ground state, in which case one might expect the N=20 magic number to still hold in this region. By measuring the longitudinal momentum distribution

of ^{29}F [9], the evolution of nuclear halo structure at the neutron drip-line can be studied. Such a measurement can be used for ^{29}F to identify which orbitals the valence neutrons are residing in, and therefore determine whether the magic number N=20 holds or breaks down. Therefore, one needs experimental information to understand which of these views is correct.

Before this can be further studied, ^{29}F must first be produced through the collision of a beam of a stable nucleus with a target. In this fragmentation, many unwanted isotopes are also produced from which ^{29}F needs to be identified and separated. An explanation of how a fragment separator works and how it is used to produce ^{29}F will be discussed in the following sections. Additionally, how the fragment separator was optimized for ^{29}F based on the analysis of simulation results of the fragment production and separation will also be discussed.

2 Fragment Separation

Nuclei near the drip-line such as ^{29}F, which has a half-life of only $\approx$2.4 ms, are created in neutron rich environments in the universe but are non-existent on Earth. Therefore, they have to be produced in a laboratory. ^{29}F can be produced through the collision of a ^{48}Ca beam with a ^{9}Be target, as shown in the reaction

$$^{48}Ca +^{9}Be \rightarrow^{29}F + X, \tag{1}$$

where X represents some of the other isotopes that are produced. When this collision occurs, many isotopes are produced from which ^{29}F needs to be identified and separated. A simulation of how this will be done using the BigRIPS fragment separator and particle detectors at the RIKEN RI Beam Factory in Japan, shown in Figure 4, was studied using the LISE++ simulation tool.

The fragment separator is used to isolate a particular nucleus of interest, in this case ^{29}F, by cutting out unwanted contaminants. It consists of a target followed by a series of dipole and quadrupole magnets, momentum dispersive and achromatic focal planes, and various wedge degraders and slits, which will be discussed further in the following sections.
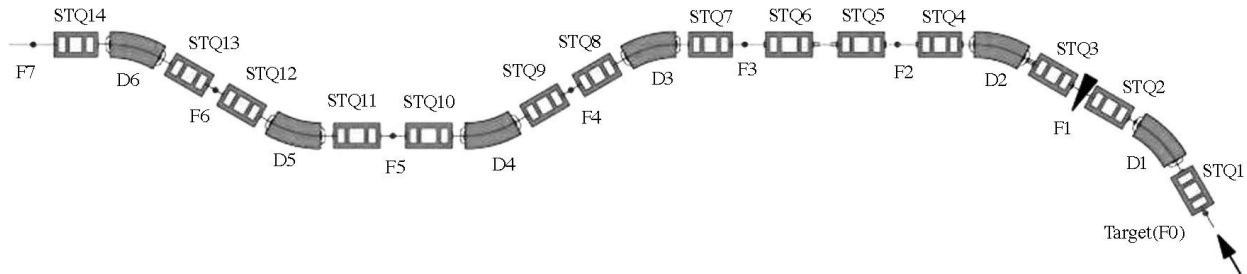

Figure 4: BigRIPS fragment separator schematic consisting of a target (F0), dipole magnets (D), quadrupole magnets (STQ), momentum dispersive focal planes (F1, F4, F5, F6), achromatic focal planes (F2, F3), and a doubly achromatic focal plane (F7) [14].

2.1 Electromagnetic Separators

Fragment separators contain electromagnetic separators, which most commonly consist of magnetic dipoles and quadrupoles [15]. Dipole magnets are used to both bend a beam around a corner to transport the ions to a specific location, as well as to disperse the beam so that only those ions within a certain range of magnetic rigidities will be accepted. Conversely, quadrupole magnets are used to focus the beam in either the vertical or horizontal plane while defocussing it in the other. A quadrupole triplet can be used to focus the beam in both the horizontal and vertical plane. To achieve this, electromagnetic separators use the Coulomb and Lorentz forces to bend the ions. The equation is given by

$$\vec{F} = \frac{d\vec{p}}{dt} = q(\vec{E} + \vec{v} \times \vec{B}) \tag{2}$$

where p is the momentum, q is the charge of the ion, $\vec{E}$ is the electric field, $\vec{v}$ is the ion's velocity, and $\vec{B}$ is the magnetic field.

This principle can be used to isolate nuclei, as their trajectory is based on their electric and/or magnetic rigidity [16]. The magnetic and electric rigidity of a fragment determines the effect that a magnetic or electric field will have on the movement of this charged particle [17]. Magnetic and electric rigidity are defined as

$$B\rho = \frac{p}{q} = \frac{\gamma m_0 \beta c}{q} = \frac{\gamma A \beta c}{Z} \tag{3}$$

$$E\rho = \frac{pv}{q} = \frac{\gamma m_0 (\beta c)^2}{q} = \frac{\gamma A (\beta c)^2}{Z} \tag{4}$$

respectively, where B is the magnetic field, E is the electric field, ρ is the radius of curvature of the beam, γ is the Lorentz factor, v is the relativistic velocity, $\beta = v/c$, c is the speed of light, and A/Z is the mass to charge ratio [15].
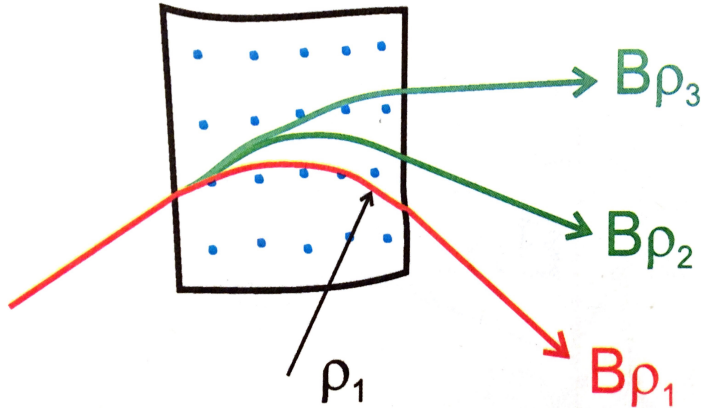

Figure 5: Separation of isotopes based on magnetic rigidities [15].

Because it relates to the momentum (p) of the particle, a particle with higher momentum or a larger A/Z ratio will have a larger radius of curvature than a particle with lower momentum or smaller A/Z ratio. However, since magnetic rigidity only separates nuclei based

on their A/Z ratio, isotopes with the same A/Z ratio have to be further separated using additional techniques.

2.2 Achromatic and Dispersive Foci

In addition to electromagnetic separators, fragment separators also have achromatic and dispersive foci, where the locations of these foci are shown in Figure 4. An achromatic focus is a focal plane in which different momenta are focused to the same position. This is shown in Figure 6, where it is labeled as F. Slits can be placed at this location to limit the acceptance in momentum width [15] and cut out unwanted contaminants. Conversely, a dispersive focus is a focal plane in which momenta corresponding to various isotopes are spatially separated, meaning that each value of momentum is spread out into different positions. This location is labeled as I in Figure 6. A wedge can be placed at this location to spatially separate isotopes based on their number of protons (Z), as is discussed in the next section.
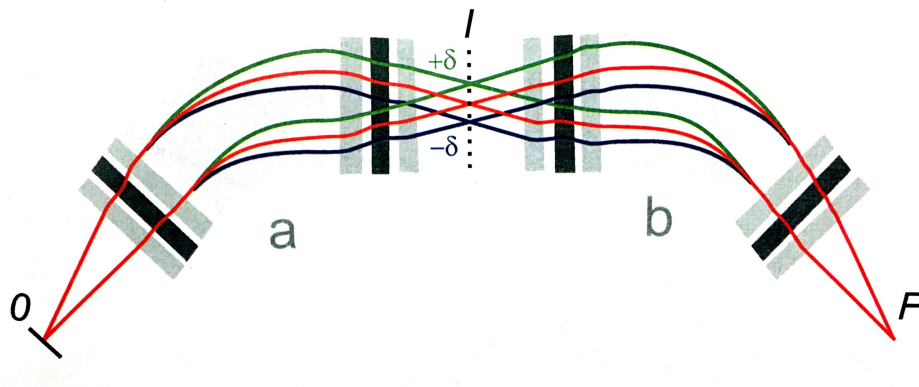

Figure 6: Both a dispersive and achromatic focal plane are shown in this figure [15], labelled as I and F respectively. The colour of each line represents a different momentum.

2.3 Wedge Degraders

To separate isotopes with the same mass to charge ratio, a wedge degrader is needed to slow them down. Because isotopes of different elements have different numbers of protons

(Z), they will have different velocities after passing through the degrader, as the slowing down is proportional to Z^2/β^2 [15]. Finally, once the isotopes are spatially separated, a slit consisting of moveable plates of a thick material can be positioned to eliminate the unwanted contaminants as they will be stopped by this material.
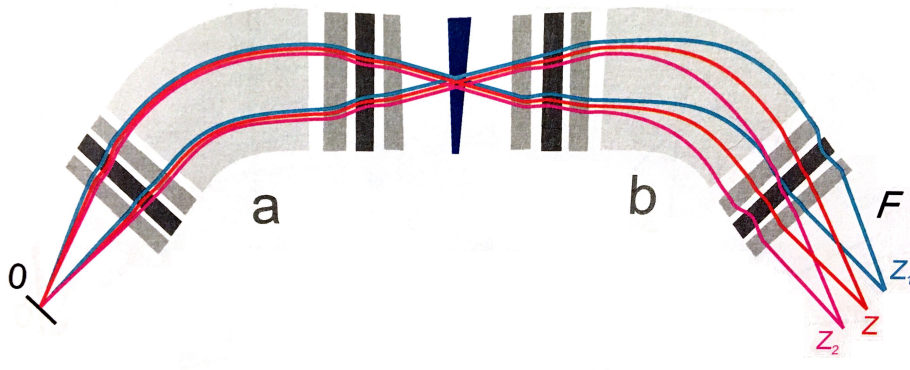

Figure 7: A wedge degrader is used to separate isotopes which have the same mass to charge ratio but have different proton numbers (Z) [15].

3   Simulation

3.1   Experimental Technique

The proposed experiment aims to measure the interaction cross section of the isotopes ^{27}F and ^{29}F to extract the matter radii for the first time [9]. In order to determine this for ^{29}F, the measurement of ^{27}F is also needed as it is the core of the Borromean halo nucleus ^{29}F. Therefore, the halo of this nucleus can then be defined, since the neutron halo is indicated by a large increase of the interaction cross section when compared to that of ^{27}F [9]. To further understand the structure of ^{29}F, the longitudinal momentum distribution after a two-neutron removal using a carbon target can be determined. In this case, the presence of a halo would be indicated by a narrow width of the inclusive momentum distribution.

To make these measurements of ^{29}F, it first needs to be produced. Using the method of In-Flight Separation, this nucleus (as well as many other fragments) can be created through the collision of a ^{48}Ca beam with a thin ^{9}Be target. In this method, the nuclei of the projectile are fragmented by the target nuclei, which produces a secondary beam. This beam then has to be separated using a fragment separator. A beam energy of 345MeV/u and intensity of 200pnA is needed to produce ^{29}F, therefore this experiment can only be carried out using the BigRIPS fragment separator and particle detectors at the RIKEN RI Beam Factory in Japan, shown in Figure 4.

The simulation tool LISE++ [18] was designed to calculate the transmission and yields of ions created through the fragmentation of a beam as it collides with a target [18]. This program can be used to simulate an experiment by defining the magnetic fields and other parameters of the fragment separator. LISE++ calculates the production rate of each fragment produced. Therefore, varying parameters such as target and wedge thicknesses, as well as slit placements, allows for the optimal settings of the fragment separator to be determined.

This program was used to simulate the experiment described above to determine the optimal settings for this fragment separator which would produce the maximum amount of ^{29}F, while greatly reducing the unwanted contaminants. In the following sections, the optimal conditions of the different parameters are described.

3.2 Effect of Target Thickness

The thickness of the ^{9}Be target, located at the point F0 in the fragment separator, corresponds to the amount of Be nuclei that are present to interact with the ^{48}Ca beam as they collide. Therefore, the thicker the target, the more ^{9}Be nuclei are available to collide with the ^{48}Ca beam. This allows for more fragments to be produced, including the nucleus of interest. To study this effect, the beam rate immediately after the target was determined.
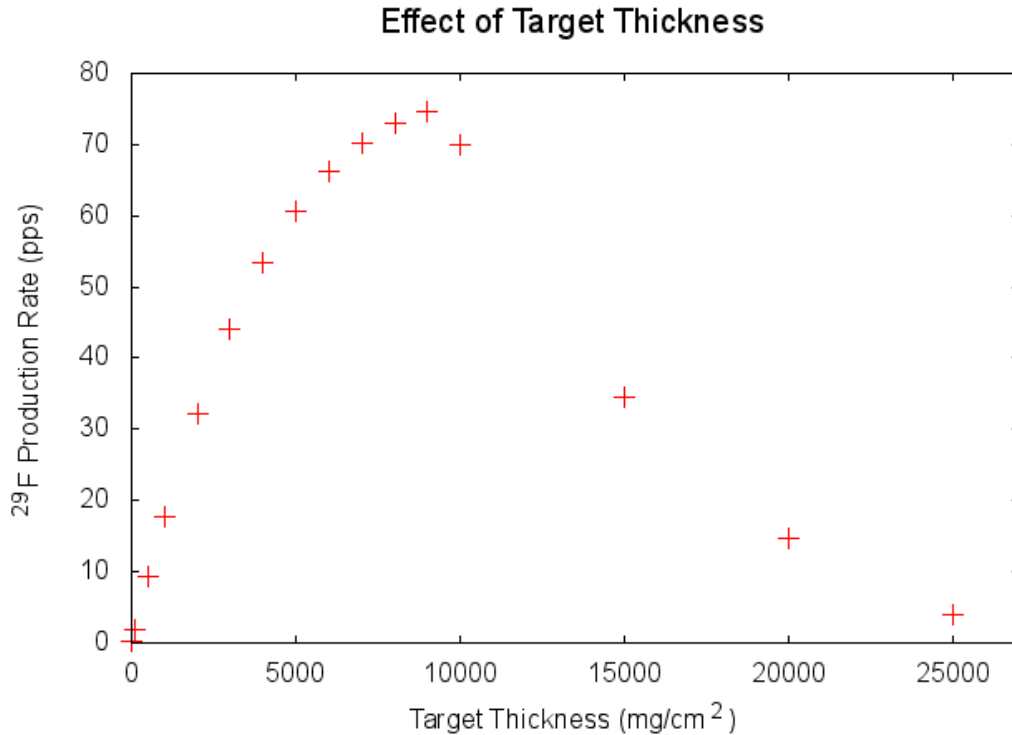
12

Figure 8: Graph showing how the production rate of ^{29}F changes as a function of target thickness at a location immediately after the target.

The graph in Figure 8 shows the production rate of ^{29}F as a function of target thickness immediately after the target, before the ions enter the fragment separator. As the target increases in thickness, more ^{29}F are produced, as is shown by the increase on the graph. However, once the target reaches a thickness of 10000 mg/cm^2, the production rate of ^{29}F starts to decline. This is due to the fact that the ions lose energy as they pass through the target. Therefore, as the target thickness increases, the ions lose more and more energy. Eventually, the target becomes too thick, causing the ions to lose all of their energy, and they are therefore unable to pass through. In addition, as the target becomes too thick, the ^{29}F produced can be lost by secondary reactions in the target.
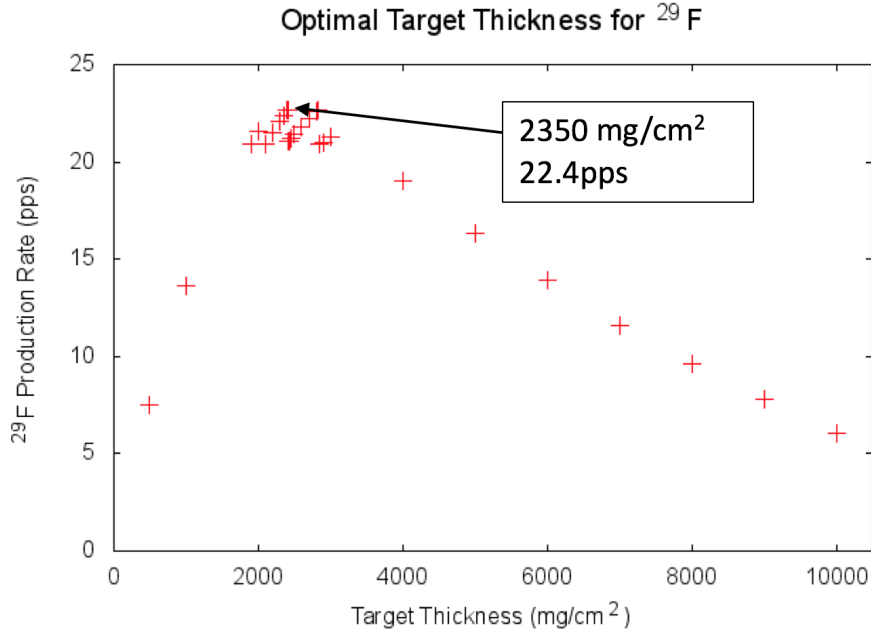
3.3   Optimal Target Thickness

Figure 9: Graph showing the optimal target thickness, which corresponds to the highest production rate of ^{29}F, which is measured after the doubly achromatic focal plane F7.

Before ^{29}F can be isolated, the magnetic rigidity ($\beta\rho$) of the spectrometer needs to be set to the allow the desired A/Z value to be the central trajectory. In the case of ^{29}F, the mass to charge ratio is $\approx$3.2. The maximum production rate for this isotope can then be determined under such $\beta\rho$ condition. To do this, the first setting that needs to be optimized is the target thickness to ensure that the initial production rate of ^{29}F is as high as possible. As shown in Figure 9, the optimal target thickness that maximized the production of ^{29}F while reducing the amount of contaminants was found to be 2350 mg/cm^2. This corresponds to a production rate of 22.4 pps for ^{29}F and a total production rate of all isotopes of $1.2{\times}10^9$ pps, shown in Figure 10.

From both Figures 9 and 10, it is shown that the production rate of ions increases until reaching a maximum, and then begins to decline. This decline is due to the broadening
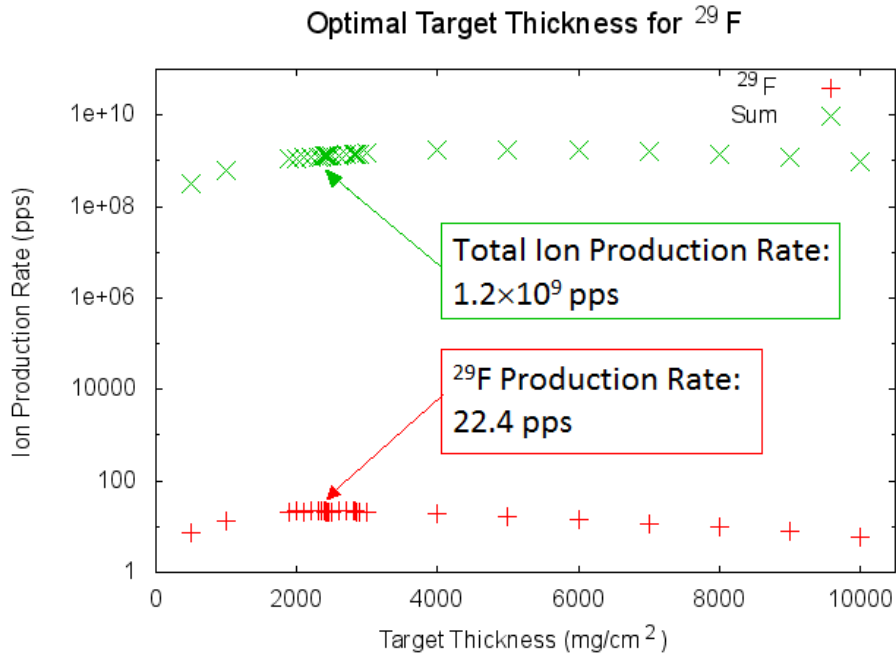
Figure 10: Graph showing the production rate of ^{29}F compared to the total ion production rate for the optimal target thickness.

of momentum, which is caused by the energy loss of the fragments as they pass through the target. As the target thickness increases, more energy is lost by the fragments, which therefore increases the broadening of the momentum. Since the fragment separator has a limited acceptance of momentum, this broadening causes more of the fragments to be cut out, therefore decreasing the production rate [17].

Figure 11 shows a particle identification plot which visually represents the contaminants that are produced along with ^{29}F, from which ^{29}F has to be separated. On this plot, horizontally placed points corresponding to each Z value represent isotopes of each element. Fluorine (F) isotopes are visible along Z=9, with oxygen (O) isotopes below and neon (Ne) isotopes above. The points that are vertically aligned in this figure correspond to isotopes of different elements that have the same mass to charge ratio. In the case of the isotope ^{29}F, the mass to charge ratio is ≈3.2, as shown.
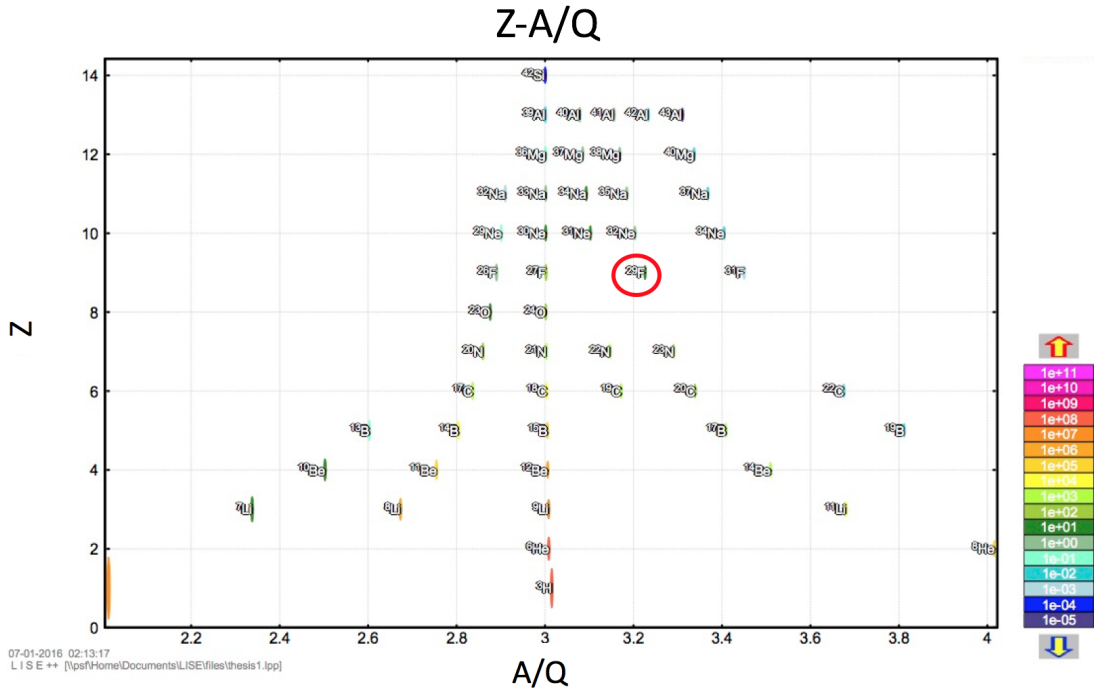
Figure 11: Particle identification plot showing ^{29}F amongst the many other fragments produced, measured after F7.
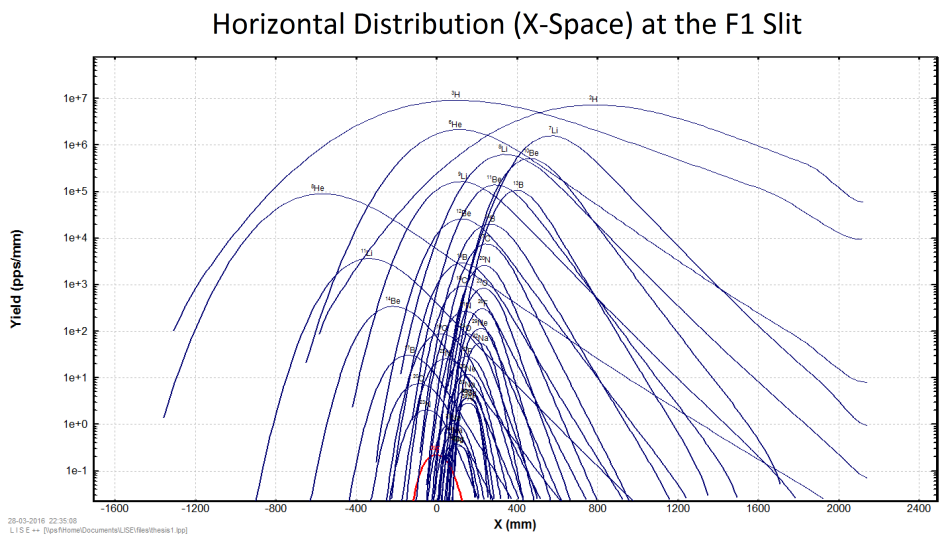
3.4 F1 Wedge Thickness

Figure 12: Plot showing the horizontal distribution of ^{29}F as well as the other contaminants. Since the production rate of ^{29}F is so small compared to that of the contaminants, it cannot be seen on this graph.

To isolate ^{29}F and decrease the amount of contaminant nuclei, a wedge degrader is needed to separate isotopes which have the same A/Z ratio by slowing them down at different rates. Without the addition of a wedge, all of the contaminant nuclei are spatially located at the same position as ^{29}F as shown in Figure 12. Since the rate of slowing down is proportional to Z^2/β^2, isotopes with different Z will have different velocities after passing through the wedge degrader. The first wedge degrader is located at F1, where the optimal thickness of this wedge was chosen to minimize the total ion production rate (sum) as much as possible, while limiting its effect on the ^{29}F production rate as shown in Figure 13. This optimal thickness was found to be 3750 mg/cm^2, which corresponds to a production rate of 17.4 pps for ^{29}F and reduces the overall amount of unwanted fragments to 6.3×10^3 pps.
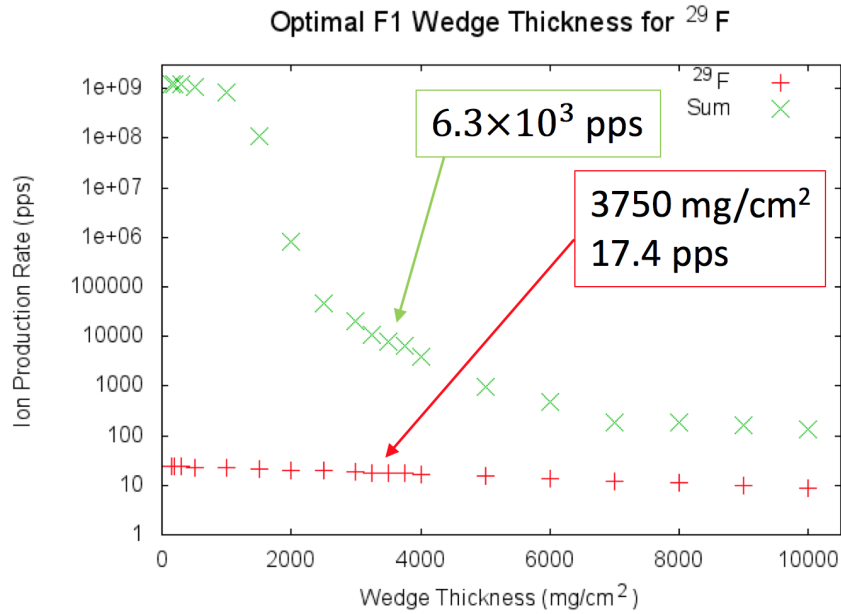
Figure 13: Graph showing the optimal F1 wedge thickness, which was chosen to decreases the total ion production rate (sum) as much as possible while minimizing its effect on the ^{29}F production rate. The slit was set to its maximum acceptance of ±50 mm.

17

3.5 F2 Slit Placement

Because the wedge degrader spatially separates the isotopes, slits can then be placed to cut out a large number of the unwanted fragments including ^{27}F, which was the fragment that was cut out the most. Based on the graph of the horizontal distribution shown in Figure 14, the F2 slit was set to ± 10 mm to limit the acceptance of the fragment separator, therefore cutting out contaminants. This drastically decreases the sum from 6.310^3 pps to only 74 pps, while the ^{29}F production rate remained at 17.4pps.
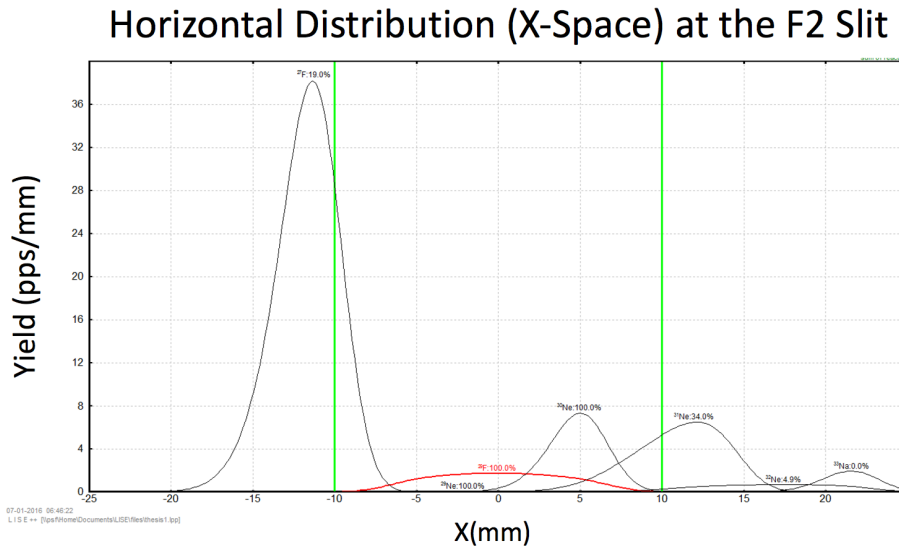

Figure 14: Plot showing the horizontal distribution of ^{29}F as well as the other contaminants. The vertical green lines represent the placement of the slit, which was used to cut out as much of the contaminants as possible while not effecting the ^{29}F production rate.

As is clear from Figure 15, a large portion of the unwanted contaminants have been moved out of the acceptance window due to the addition of the F1 wedge and F2 slit. However, since the degrader acts on all particles passing through, it also slows down ^{29}F due to momentum broadening, therefore slightly decreasing its production rate.
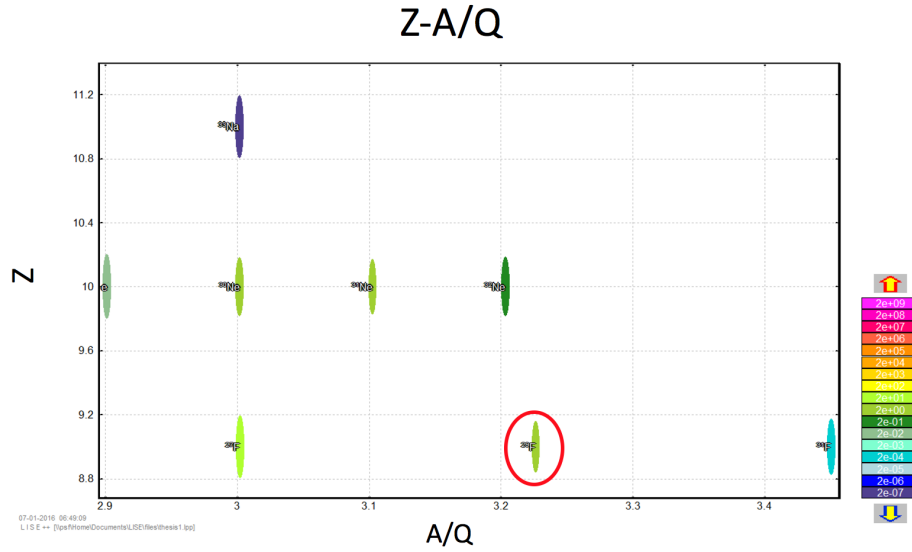
18

Figure 15: Particle identification plot showing how the addition of the F1 wedge and F2 slit greatly decreased the amount of unwanted fragments.
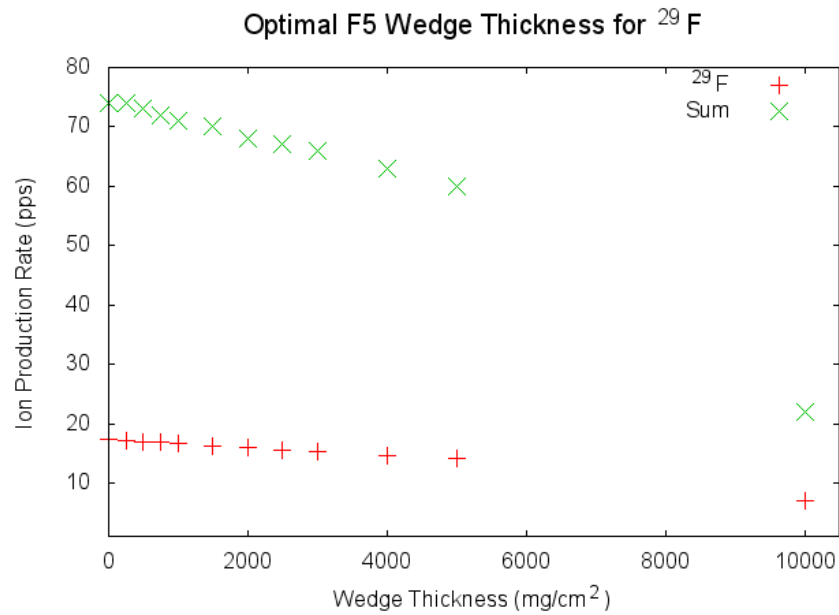
3.6 F5 Wedge Thickness

Figure 16: Since the increasing thickness of the wedge decreased the production rate of ^{29}F but did not significantly decrease the total ion production rate, the addition of this wedge was not needed.

After the majority of the contaminants are cut out by the slit, the remaining fragments can be further separated through the addition of a second wedge. However, because the total ion production rate and the production rate of ^{29}F are of the same order of magnitude after the F2 slit, as shown in Figure 16, and knowing that the addition of the wedge decreases the production rate of all isotopes including ^{29}F, it was decided that the addition of the second wedge was not necessary. In other words, since the production rate of ^{29}F decreased while the effect on the overall sum was minimal, the addition of the second wedge was not needed.
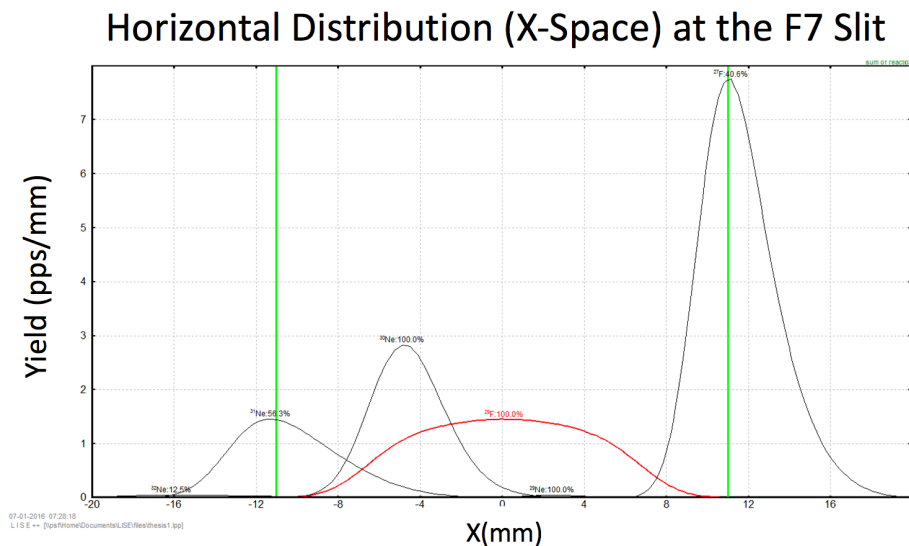
3.7 F7 Slit Placement

Figure 17: Plot showing the horizontal distribution of ^{29}F as well as the other contaminants. The vertical green lines represent the placement of the slit, which was used to cut out as much of the contaminants as possible while not effecting the ^{29}F production rate.

Although the second wedge degrader was not needed, by looking at the spatial dispersion in Figure 17, it is clear that an additional slit can be used to further decrease the amount of contaminants. Based on this position distribution, the slit located at F7 was set to ± 11 mm. This allowed for the ^{29}F production rate to remain at 17.4 pps while the total rate of

all fragment decreased to 49 pps. Analyzing the final particle identification plot shown in Figure 18, it is clear that the production rate of unwanted contaminants has been greatly reduced from what it was initially.
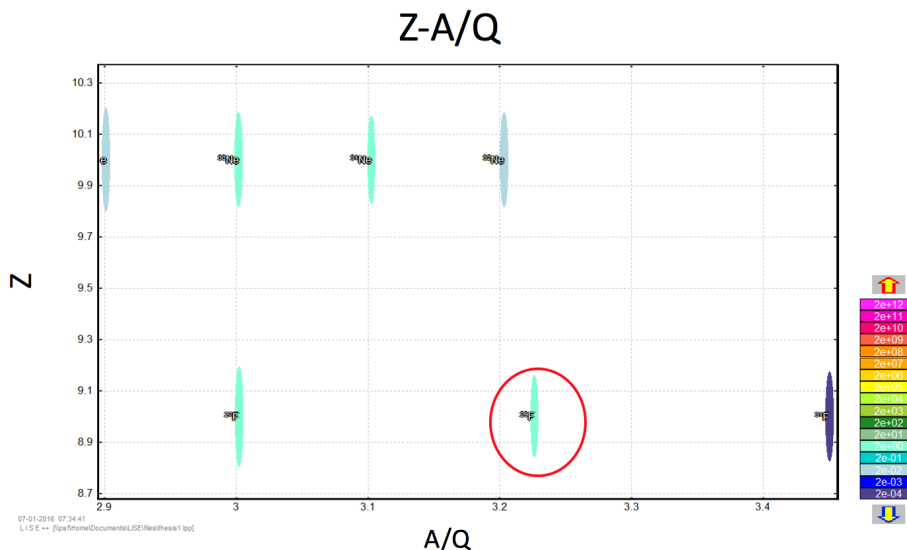

Figure 18: Particle identification plot showing how the addition of the F1 wedge and F2 slit greatly decreased the amount of unwanted fragments.

4   Conclusion

In neutron-rich nuclei such as ^{29}F, nuclear shell structure may change, and there is evidence to suggest that the magic number N=20 breaks down. Therefore, it is important to investigate the N=20 shell gap to see if it breaks down at ^{29}F, as well as whether this Borromean nucleus forms a halo. Simulation results of how ^{29}F was produced and isolated in using the BigRIPS fragment separator and particle detectors at the RIKEN RI Beam Factory in Japan were analyzed.

From this simulation, it was determined that the optimal settings of the fragment sepa-

rator, which maximized the production rate of ^{29}F while minimizing that of the unwanted contaminants, were as follows: F0 target thickness of 2350 mg/cm^2, F1 focal plane wedge thickness of 3750 mg/cm^2, F2 focal plane slit width of ± 10 mm, no wedge at F5 focal plane, and F7 focal plane slit width of ± 11 mm.

The total ion production rate and ^{29}F production rate after the optimal target thickness was determined, before any of the other settings were optimized, were found to be 1.2×10^9 pps and 22.4 pps respectively. Once the optimal wedge thicknesses and slit widths were determined, the total ion production rate was greatly reduced to 49 pps, while the production rate of ^{29}F was only reduced slightly to 17.4 pps.

By altering parameters such as target thickness, wedge thickness, and slit widths, the fragment separator has been optimized to isolate ^{29}F. Additionally, the production rate of ^{29}F was maximized, while that of the contaminants was minimized. Now that ^{29}F has been separated, it can be further investigated.

References

[1] Mayer, M. G. On Closed Shells in Nuclei. II. Physical Review 75, 19691970 (1949).

[2] Kanungo, R. *A new view of nuclear shells.* Physica Scripta T152, 014002 (2013).

[3] Feenberg, E. & Hammack, K. C. *Nuclear Shell Structure.* Physical Review 75, 18771893 (1949).

[4] Pryce, M. H. L. *Nuclear Shell Structure.* Reports on Progress in Physics 17, 134 (1954).

[5] Sonzogni, A. *Interactive Chart of Nuclides.* http://www.nndc.bnl.gov/chart/

[6] Otsuka, T. et al. *Magic Numbers in Exotic Nuclei and Spin-Isospin Properties of the NN Interaction.* Physical Review Letters 87, (2001).

[7] Dobaczewski, J., Hamamoto, I., Nazarewicz, W. & Sheikh, J. A. *Nuclear shell structure at particle drip lines.* Physical Review Letters 72, 981984 (1994).

[8] Riisager, K. *Nuclear halo states.* Reviews of Modern Physics 66, 11051116 (1994).

[9] Kanungo, R. *Proton and matter radii and momentum distribution of Borromean nuclei at the neutron drip-line.* (2014).

[10] Lunney, D. (2004, May 4). *ISOLDE goes on the trail of superlatives.* http://cerncourier.com/cws/article/cern/29077

[11] Utsuno, Y., Otsuka, T., Mizusaki, T. & Honma, M. *Extreme location of F drip line and disappearance of the N = 20 magic structure.* Physical Review C 64, (2001).

[12] Caurier, E., Nowacki, F. & Poves, A. *Merging of the islands of inversion at N = 20 and N = 28.* Physical Review C 90, (2014).

[13] Gaudefroy, L. et al. *Direct Mass Measurements of B 19 , C 22 , F 29 , Ne 31 , Na 34 and Other Light Exotic Nuclei.* Physical Review Letters 109, (2012).

[14] *Accelerator-Overview.* http://www.nishina.riken.jp/RIBF/BigRIPS/overview.html

[15] Baumann, T. *Minicourse on Experimental Techniques at the NSCL: Fragment Separators.* (2001)

[16] Winger, J. A., Sherrill, B. M. & Morrissey, D. J. *INTENSITY: a computer program for the estimation of secondary beam intensities from a projectile fragment separator.* Nuclear Instruments and Methods in Physics Research Section B: Beam Interactions with Materials and Atoms 70, 380392 (1992).

[17] Poenaru, D. & Greiner, W. *Experimental Techniques in Nuclear Physics.* (Walter de Gruyter, 1997).

[18] LISE++: Exotic Beam Production with Fragment Separators. (n.d.). Retrieved from http://lise.nscl.msu.edu/lise.html